Nano Research

Open Access

Research Article

Ultralow-force-driven polarization switching in molecular ferroelectrics

Tai-Ting Sha[1,§], Qiang Pan[1,§] ✉, Zi-Jie Feng[1,§], Xiang Zhang[2], Xiao-Xing Cao[1], Yu-An Xiong[1], Hao-Ran Ji[1], Ru-Jie Zhou[1], Wen Zhang[1] ✉, Huihui Hu[1] ✉, and Yu-Meng You[1] ✉

[1] *Jiangsu Key Laboratory for Science and Applications of Molecular Ferroelectrics, Southeast University, Nanjing 211189, China*
[2] *Jiangsu Key Laboratory for Design and Manufacture of Micro-Nano Biomedical Instruments, School of Mechanical Engineering, Southeast University, Nanjing 211189, China*
[§] *Tai-Ting Sha, Qiang Pan, and Zi-Jie Feng contributed equally to this work.*

Cite this article: *Nano Research*, **2026**, *19*, 94908742. https://doi.org/10.26599/NR.2026.94908742

ABSTRACT: Manipulation of ferroelectric domains is essential for advancing ferroelectric electronics. Mechanical switching offers an effective route for nanoscale domain control, yet conventional inorganic ferroelectrics typically require micronewton-level forces applied by nanoscale probes, generating GPa local pressures that risk material damage and make it challenging to mechanically generate large-area ferroelectric domain patterns. Overcoming this limitation demands ferroelectrics capable of responding to extremely small mechanical stimuli. Here, we demonstrate ultralow-force-driven polarization switching in the molecular ferroelectric (3,3-difluorocyclobutylammonium)$_2$CuCl$_4$, a two-dimensional organic–inorganic hybrid perovskite. Domain switching is achieved with an applied force of only 25 nN—corresponding to a local pressure below 20 MPa, orders of magnitude lower than that required for inorganic oxide ferroelectrics. This exceptionally low mechanical threshold arises from the intrinsic structural compliance and flexibility of molecular ferroelectrics. Moreover, the remarkably small switching force also enables ultrasound-driven domain modification. These results create new opportunities for molecular ferroelectrics in mechanoelectrical electronics, energy harvesting, and ultrasonic catalysis.

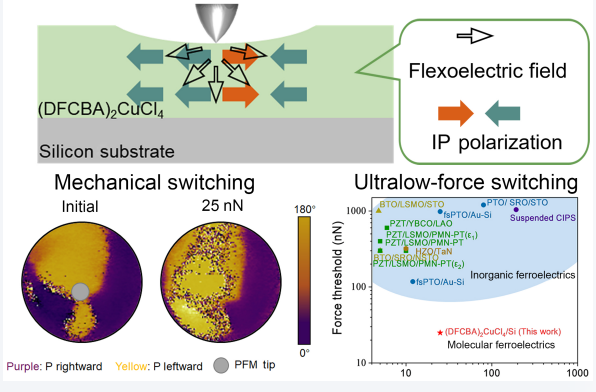

KEYWORDS: mechanical domain switching, organic–inorganic hybrid perovskite, molecular ferroelectrics, flexoelectricity

1 Introduction

The study of emerging high-quality ferroelectric nanomaterials presents exciting opportunities for the development of miniaturized high-density ferroelectric electronic devices, lightweight sensors, and flexible transducers [1–6]. In these materials, domains and domain walls critically influence nearly all physical properties, making device performance highly sensitive to domain configurations and underscoring the importance of precise domain control for optimizing functionality [7–11]. While electric fields remain the most widely used and effective approach for switching ferroelectric domains, their application at the nanoscale faces challenges such as leakage currents, dielectric breakdown, and surface damage caused by ionic migration [12–14].

Mechanical switching has emerged as an attractive alternative, offering intrinsic advantages including sub-100-nm spatial resolution, electrode-free processes, and compatibility with a broad range of device architectures [14–16]. Such mechanical switching has been demonstrated in various inorganic oxide ferroelectrics, including $BaTiO_3$ [13, 17], $BiFeO_3$ [12], $PbTiO_3$ [18], $Pb(Zr,Ti)O_3$ [19–21], and $Hf_{0.5}Zr_{0.5}O_2$ [16]. However, their intrinsic lattice rigidity necessitates micronewton-level forces applied by nanoscale AFM probes to induce polarization reversal [12, 13, 16, 18–21]. These forces correspond to local pressures of several GPa. Such extreme stresses pose the risk of irreversible lattice damage and plastic deformation [20–22], and greatly limit the feasibility of mechanically creating large-area ferroelectric domain patterns, thereby restricting the practical applications of mechanical

Received: December 30, 2025; **Revised:** April 15, 2026
Accepted: April 17, 2026

✉Address correspondence to Qiang Pan, pq@seu.edu.cn; Wen Zhang, zhangwen@seu.edu.cn; Huihui Hu, huhuihui@seu.edu.cn; Yu-Meng You, youyumeng@seu.edu.cn

switching. Overcoming this limitation requires ferroelectrics with much higher mechanical sensitivity.

In recent years, the renaissance of molecular ferroelectrics is believed to be a promising pathway for achieving ultralow-force domain switching. Their soft lattice frameworks, structural adaptability, low density, and facile solution processing collectively endow them with exceptional mechanical compliance [23–25]. Representative examples, such as N-ethyl-N-(fluoromethyl)-N-methylethylammonium tetrabromoferrate(III) [26], (3-F-Q)ReO_4 [27], and 2-(hydroxymethyl)-2-nitro-1,3-propanediol [28], have demonstrated unusual functionalities such as giant strain-enhanced piezoelectricity, ultralow hardness, and 24-fold polar axes. Despite these advances, force-induced switching in molecular ferroelectrics has not yet been demonstrated, primarily due to the limited studies on nanometer-thick molecular ferroelectric materials.

Here, we report ultralow-force-driven polarization switching in the two-dimensional molecular ferroelectric $(DFCBA)_2CuCl_4$ (DFCBA = 3,3-difluorocyclobutylammonium). Freestanding nanosheets (NSs) synthesized via an antisolvent method exhibit great in-plane (IP) ferroelectricity. Remarkably, polarization reversal is achieved using an applied force of only 25 nN—corresponding to a local pressure below 20 MPa, which is orders of magnitude lower than the switching forces required in conventional inorganic oxide ferroelectrics. The extremely low force threshold originates from the intrinsic structural compliance and flexibility of the molecular lattice, which enables the generation of large strain gradients and strong flexoelectric fields under minimal stress. Such an ultralow mechanical threshold enables ultrasound-driven domain modification. This capability opens avenues for integrating molecular ferroelectrics into mechanoelectrical electronics, energy harvesting, and ultrasound-mediated catalysis.

2 Results and discussion

2.1 Preparation and characterization of $(DFCBA)_2CuCl_4$ NSs

$(DFCBA)_2CuCl_4$ crystallizes in the monoclinic polar C_c space group at 293 K in the ferroelectric phase. The crystal structure consists of inorganic $(CuCl_4)^{2-}$ layers of corner-sharing $CuCl_6$ octahedra, interspersed with organic $(DFCBA)^+$ bilayers (Fig. 1(a)), forming a two-dimensional (2D) organic–inorganic A_2BX_4 perovskite structure. In this structure, $(DFCBA)^+$, Cu^{2+}, and Cl^- correspond to the A, B, and X sites, respectively [29]. Additionally, weak N–H···Cl hydrogen bonds are present between the inorganic and organic components, with an average donor–acceptor distance of 3.350 Å. The $(DFCBA)^+$ cations enhance the colloidal stability of the nanosheets and prevent the $CuCl_6$ octahedra from forming a three-dimensional framework, which is beneficial to the synthesis of $(DFCBA)_2CuCl_4$ NSs [30, 31]. The polar $(DFCBA)^+$ cation exhibits an orientational arrangement along the *c* axis, with the C–N groups of the $(DFCBA)^+$ cations aligned along the *c* axis, thereby inducing polarization. At 393 K, in the paraelectric phase, the crystal symmetry of $(DFCBA)_2CuCl_4$ transitions to the tetragonal

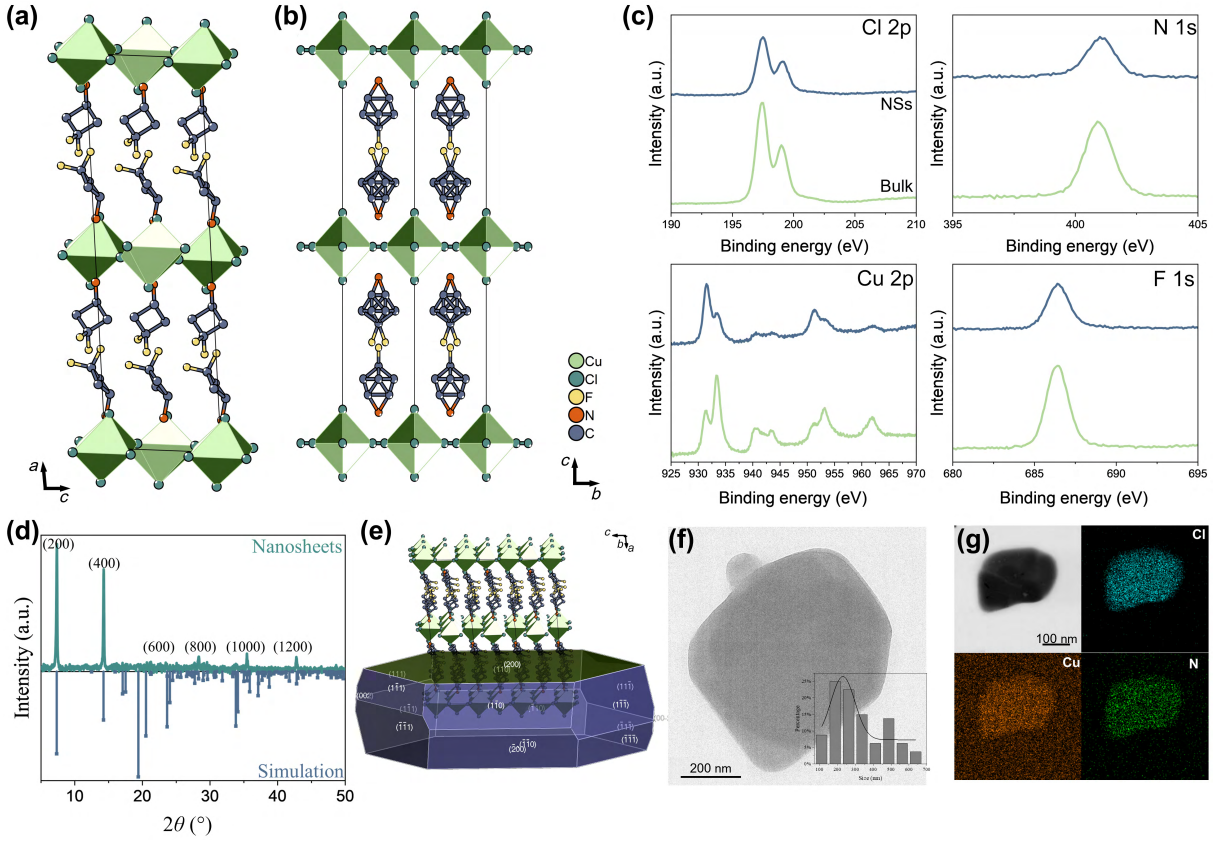

Figure 1 Crystal structure and characterization of $(DFCBA)_2CuCl_4$ NSs. Crystal structures of the layered perovskite $(DFCBA)_2CuCl_4$ in (a) ferroelectric and (b) paraelectric phases. (c) XPS patterns of the $(DFCBA)_2CuCl_4$ NSs (top) and bulk crystal (bottom). (d) XRD patterns of the $(DFCBA)_2CuCl_4$ NSs and simulated patterns of the bulk crystal. (e) Simulated morphology of the single crystal $(DFCBA)_2CuCl_4$. The largest exposed facet (200) is colored green. (f) Representative TEM image and corresponding lateral size distribution of $(DFCBA)_2CuCl_4$ NSs. (g) STEM image and EDS elemental mappings of $(DFCBA)_2CuCl_4$ NSs.

centrosymmetric $P4_2/mmc$ space group, in which both the inorganic and organic components become highly disordered [29, 32] (Fig. 1(b)). According to Aizu notation [33], the phase transition in $(DFCBA)_2CuCl_4$ corresponds to the 4/*mmmFm* ferroelectric transition. During this process, the symmetry is reduced from 16 elements in the 4/*mmm* (D_{4h}) point group to just 2 elements in the *m* (C_{1h}) point group. As a result, $(DFCBA)_2CuCl_4$ is classified as a multiaxial ferroelectric, possessing four ferroelectric axes and eight equivalent polarization directions [29].

In this work, ferroelectric $(DFCBA)_2CuCl_4$ nanosheets were synthesized at room temperature using a highly repeatable antisolvent method [30, 34], as previously reported [31] (Fig. S1 in the Electronic Supplementary Material (ESM)). A DMF precursor solution containing $CuCl_2$ and (DFCBA)Cl (1:2 molar ratio) was rapidly added into vigorously stirred toluene at room temperature, resulting in the immediate formation of $(DFCBA)_2CuCl_4$ nanosheets due to the sudden drop in solubility. This formation was visually confirmed by a color change from colorless to yellow-green (Fig. S2 in the ESM). X-ray photoelectron spectroscopy (XPS) was performed to analyze the surface composition of $(DFCBA)_2CuCl_4$ nanosheets and their bulk crystal counterpart. As shown in Fig. 1(c), the Cl 2p, N 1s, Cu 2p, and F 1s spectra of the NSs exhibit binding energy positions comparable to those of the bulk crystals, confirming the presence of both $CuCl_2$ and $(DFCBA)^+$ components. The Cl 2p region can be fitted into two peaks at 197.4 eV ($2p_{3/2}$) and 199.1 eV ($2p_{1/2}$). The Cu $2p_{3/2}$ peak at 933.3 eV, along with strong satellite features at 940 and 962 eV, indicates the presence of Cu^{2+}. However, X-ray irradiation during XPS measurements can partially reduce Cu^{2+} to Cu^+, as evidenced by the Cu^+ $2p_{3/2}$ peak at 931.5 eV observed in both NSs and bulk samples [35]. Notably, due to their significantly larger specific surface area, the NSs exhibit a stronger Cu^+ $2p_{3/2}$ signal, indicating a higher degree of surface reduction.

X-ray diffraction (XRD) was performed on drop-cast films of the nanosheets to investigate their structure and purity. The sharp diffraction peaks observed (Fig. 1(d)), which closely match the simulated pattern, confirm the high crystallinity and purity of the nanosheets. The periodic (*h*00) diffraction peaks (*h* = 2, 4, 6, 8, 10, and 12) indicate vertical stacking of the nanosheets. Specifically, nanosheets lie flat on the substrate and overlap, with preferred orientation along the (*h*00) family of planes, consistent with previous reports [31, 36]. This result also agrees with our simulated crystal growth, which predicts (200) as the dominant exposed facet (Fig. 1(e)). Figure 1(f) shows representative transmission electron microscopy (TEM) images of $(DFCBA)_2CuCl_4$ nanosheets, revealing lateral dimensions of several hundred nanometers, with an average size of ~ 313 nm. The corresponding energy dispersive X-ray spectroscopy (EDS) spectrum (Fig. S3 in the ESM) confirms the presence of C, N, F, Cu, and Cl elements. Elemental mapping (Fig. 1(g)) further demonstrates the uniform distribution of N, Cu, and Cl across the nanosheets. Due to the strong electron-beam sensitivity of the hybrid perovskite nanosheets, TEM-based diffraction analysis could not be reliably performed [37, 38], precluding direct determination of the in-plane crystallographic orientation of individual nanosheets.

2.2 Electrical polarization switching

Piezoresponse force microscopy (PFM) measurements reveal that the as-synthesized $(DFCBA)_2CuCl_4$ nanosheets exhibit a multidomain state. As shown in Figs. 2(a) and 2(b), the pristine domain pattern of a single NS (thickness = 46 nm) displays clear domain walls, visible as low-amplitude regions (dark lines) in the PFM amplitude image, while the vertical PFM response was negligible, owing to the weak out-of-plane (OP) polarization component. Powder X-ray diffraction (PXRD) analysis confirms that the nanosheets preferentially expose the (200) plane, defining the out-of-plane crystallographic reference for PFM measurements. The IP PFM signal therefore reflects polarization components within this plane, projected perpendicular to the cantilever. To investigate the electrical domain switching behavior of $(DFCBA)_2CuCl_4$ NSs, we manipulated the spontaneous polarization by scanning with an electrically biased PFM tip. The tip was scanned at +4.4 V along the blue dashed arrow at a speed of 100 $nm{\cdot}s^{-1}$, inducing in-plane polarization reversal via the trailing electric field [39]. As shown in the PFM phase image (Fig. 2(e)), the purple domain expanded along the scanning direction, indicating polarization switching from rightward to leftward polarization. Furthermore, the switched domains remained stable for over 12 h (Fig. S4 in the ESM), thereby ruling out possible artifacts arising from charge injection. Repeating the scan with –4.4 V reversed the polarization back to its original state (Fig. 2(g)), confirming reversible domain switching. Additionally, switching spectroscopy PFM was performed on another NS (thickness = 40 nm). Upon applying a triangular voltage pulse exceeding the coercive field, a clear 180° phase shift was observed, accompanied by a butterfly-shaped amplitude response (Fig. 2(h)). These results provide clear evidence of reversible polarization switching and ferroelectric behavior in $(DFCBA)_2CuCl_4$ nanosheets, indicating their relatively low coercive field.

2.3 Nanonewton-level mechanical polarization switching

A schematic illustration of mechanical domain switching is shown in Fig. 3(a). $(DFCBA)_2CuCl_4$ nanosheets were spin-coated onto silicon substrates and annealed (Fig. S5 in the ESM). An electrically grounded AFM tip was positioned at the center of a nanosheet to apply a vertical force at a single point, controlled via the AFM force-curve mode. The applied force was held for 1 s before unloading. To ensure accurate force quantification, the spring constant and the inverse optical lever sensitivity of the AFM cantilever were calibrated using the thermal noise and force-curve methods via the *GetReal* function in the Asylum Research software (Fig. S6 in the ESM) [15, 40]. PFM imaging was performed both before and after force application to compare the evolution of ferroelectric domains. To minimize interference to ferroelectric domains, a typical contact force during PFM imaging is ~ 20 nN.

We conducted a series of experiments on $(DFCBA)_2CuCl_4$ nanosheets with thicknesses ranging from 25 to 220 nm. The full sequence of domain evolution under increasing applied forces for a 25 nm-thick nanosheet is presented in Fig. 3(c). As shown in Fig. 3(c), during the first three scans, in which the applied force was ≤ 20 nN, only minor variations in domain shape were observed. These slight changes are likely attributed to the thermal drift of PFM imaging at the nanoscale [41]. In contrast, after a force of 25 nN was applied for 1 s prior to the fourth scan, a pronounced change in the domain configuration was observed, with the left-side domain disappearing completely. These results indicate that IP PFM imaging performed with a contact force of ~ 20 nN does not significantly contribute to domain evolution. Instead, the observed domain switching is consistent with a mechanically induced effect arising from a sufficiently large force, rather than from repeated

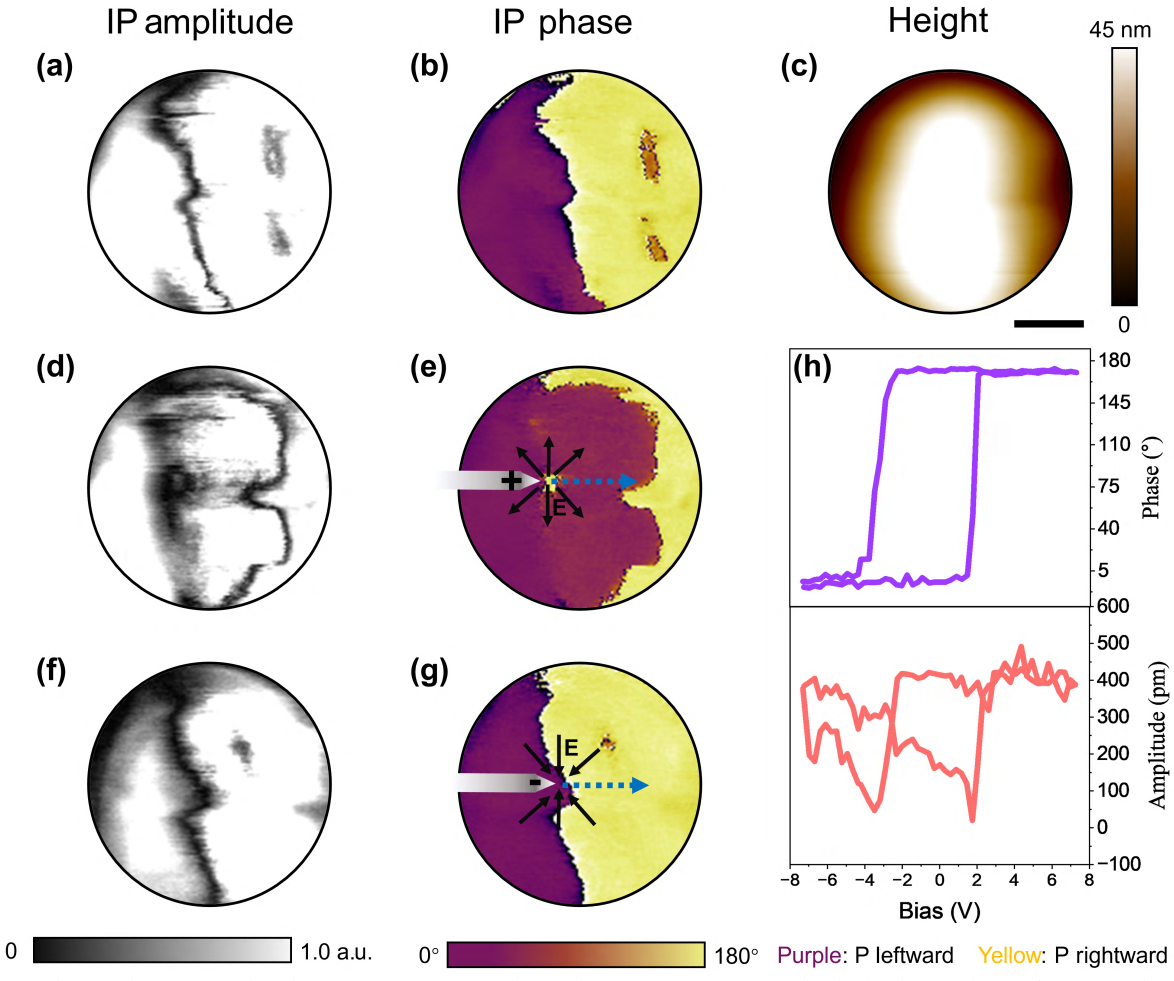

Figure 2 Ferroelectric polarization switching by PFM on $(DFCBA)_2CuCl_4$ NSs. The pristine IP PFM (a) amplitude, (b) phase, and (c) surface topography images of a single NS. (d) PFM amplitude and (e) phase images after moving the PFM tip along the blue dashed arrow with a tip bias of +4.4 V and a speed of 100 nm·s^{-1}. (f) PFM amplitude and (g) phase images after moving the PFM tip along the blue dashed arrow with a tip bias of −4.4 V and a speed of 100 nm·s^{-1} for domain back-switching. (h) Off-field local lateral PFM-switching spectroscopy of the phase (top) and amplitude (bottom). Scale bar: 200 nm. The color contrast represents relative in-plane polarization projections perpendicular to the cantilever under a fixed scan geometry.

PFM scanning. This mechanical switching behavior was consistently observed in nanosheets with various thicknesses, demonstrating its robustness. Additional examples of ferroelectric domain evolution under increasing applied forces are provided in Fig. S7 in the ESM. Topography images of the nanosheets before and after mechanical switching (Fig. S8 in the ESM) indicate that the mechanical switching process did not induce any noticeable morphological changes. Notably, the threshold force required for switching increases significantly in the thicker flakes [15] (Fig. 3(b)). This thickness dependence is governed by the distribution of strain gradients through the film, which determines the resulting flexoelectric field, as well as by surface polarization relaxation [42]. This mechanism leads to a nontrivial evolution rather than a simple scaling law [43, 44]. Therefore, we describe the result conservatively as a clear monotonic increase of the switching force with thickness within the measured range, without assigning a strictly linear or quadratic dependence.

Remarkably, even for nanosheets several hundred nanometers thick, switching could still be achieved under forces of only a few hundred nanonewtons, underscoring the material's exceptional mechanical switchability. Notably, although the AFM tip geometry and loading conditions are almost symmetric, the resulting switching behavior in our experiments does not occur symmetrically on both sides of the tip. Specifically, the $(DFCBA)_2CuCl_4$ nanosheets exhibit spatially asymmetric domain evolution, with switching preferentially occurring on one side. This behavior is likely associated with practical factors such as slight structural inhomogeneities (e.g., thickness variations or local defects), which can lead to an uneven strain-gradient distribution beneath the tip. Furthermore, unlike many prior mechanical switching studies performed in single-domain regions, the nanosheets investigated here are mostly multidomain under the present synthesis conditions (representative IP PFM images of as-grown nanosheets are provided in Fig. S9 in the ESM), and the pre-existing domain configuration can influence the local switching pathway, contributing to the observed asymmetry.

2.4 Mechanism of mechanical switching and ultralow switching force

Figures 4(a) and 4(b) illustrate the mechanism of mechanical switching in our experiments. The applied stress from the PFM tip generates an outward IP flexoelectric field—analogous to the effect of a positively biased tip [12, 22]. Incorporating the IP flexoelectric field into the Landau free energy breaks the symmetry of the double-

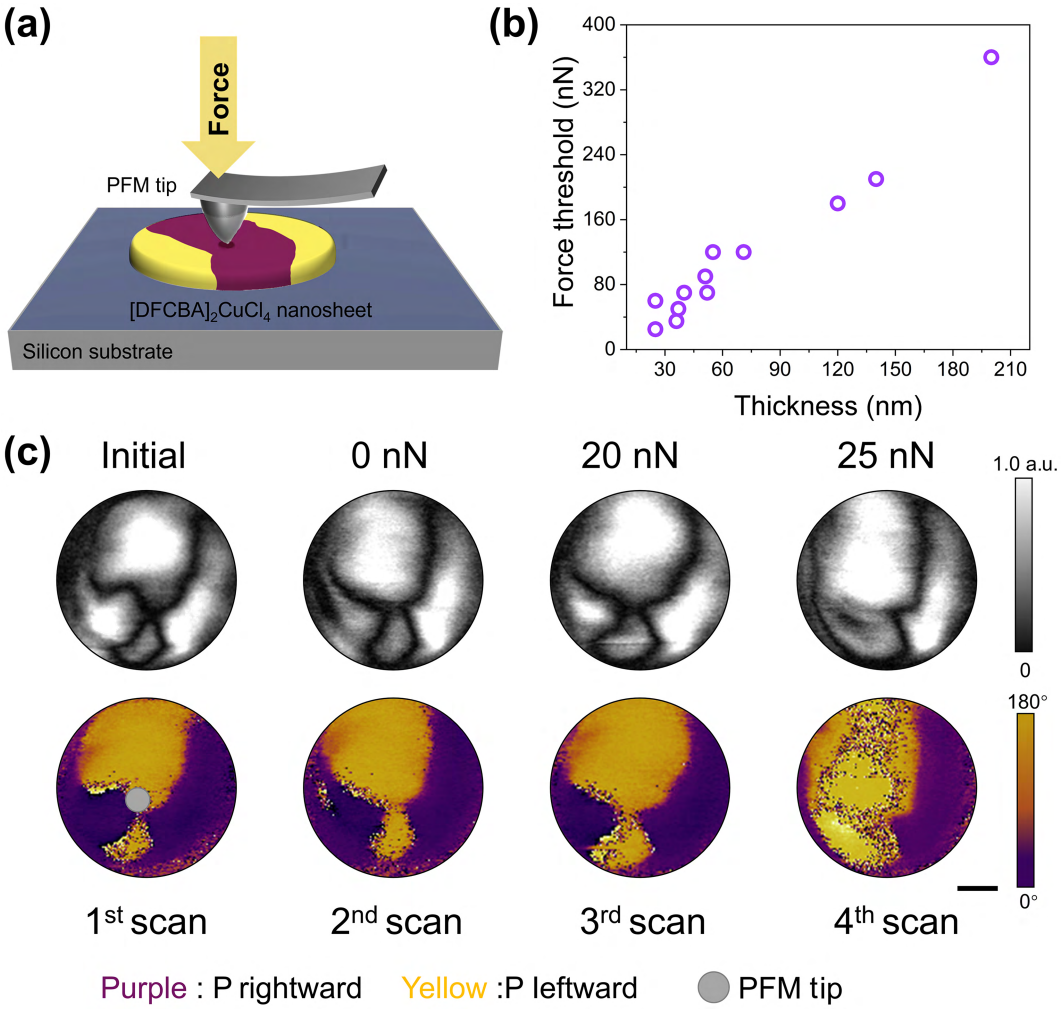

Figure 3 Nanonewton-level force-induced polarization switching on $(DFCBA)_2CuCl_4$ NSs. (a) A schematic of the mechanical domain switching setup. (b) Switching force threshold as a function of the nanosheets thickness. (c) The IP domain structures of a NS with a thickness of 25 nm PFM images after applying increasing forces from 0 to 25 nN for 1 s. Scale bar: 100 nm. The color contrast represents relative in-plane polarization projections perpendicular to the cantilever under a fixed scan geometry.

well potential [13, 15, 16, 22] (Fig. 4(b)), introducing an energy difference between leftward and rightward polarizations and enabling switching toward the lower-energy state via the flexoelectric effect. When the applied stress is sufficiently large, the resulting flexoelectric field becomes strong enough to drive polarization reversal. According to the analysis by Park et al. [12], the flexoelectric field generated under mechanical loading can exhibit a relatively strong IP component, whereas the electric field produced by a biased AFM tip is typically dominated by the OP component, with a comparatively weaker IP component. This difference in field distribution may help explain the experimentally observed in-plane polarization switching under mechanical loading in our system.

We further compared the threshold force required for domain switching in our samples with previously reported values for inorganic ferroelectric membranes [12, 13, 15–22, 43, 45] (Fig. 4(c)). The data reveals a clear trend: the required tip pressure decreases as membrane thickness is reduced. From a practical perspective, fabricating and integrating high-quality ultrathin ferroelectric membranes remains technically challenging. Therefore, achieving reliable mechanical switching in relatively thicker membranes is of particular significance for device applications. Remarkably, an ultralow switching force of just 25 nN was achieved in 25 nm-thick $(DFCBA)_2CuCl_4$ nanosheets on silicon—representing the lowest switching force reported to date, even lower than that of thinner membranes.

In conventional inorganic perovskites (ABO_3), the BO_6 framework is sustained by B–O bonds with mixed ionic-covalent character, forming a rigid three-dimensional network that governs the elastic response and gives rise to the high stiffness characteristic of oxide ferroelectrics. Such strong lattice bonding makes structural distortion energetically costly [46]. In contrast, layered hybrid perovskites $(DFCBA)_2CuCl_4$ consist of inorganic slabs separated by organic components that are linked through much weaker intermolecular interactions (hydrogen bonding and van der Waals forces) [29, 47, 48]. This bonding arrangement results in a pronounced structural anisotropy and accessible intermolecular slip pathways, collectively enabling greater mechanical compliance and deformability. Nanoindentation measurements (Fig. S10 in the ESM) reveal an elastic modulus of only 7.2 GPa—significantly lower than that of typical inorganic oxide ferroelectrics, which commonly exceed 100 GPa [49–53], and even lower than that of the two-dimensional van der Waals ferroelectric CIPS (27 GPa) [54]. According to previous reports [12, 43], the mechanical

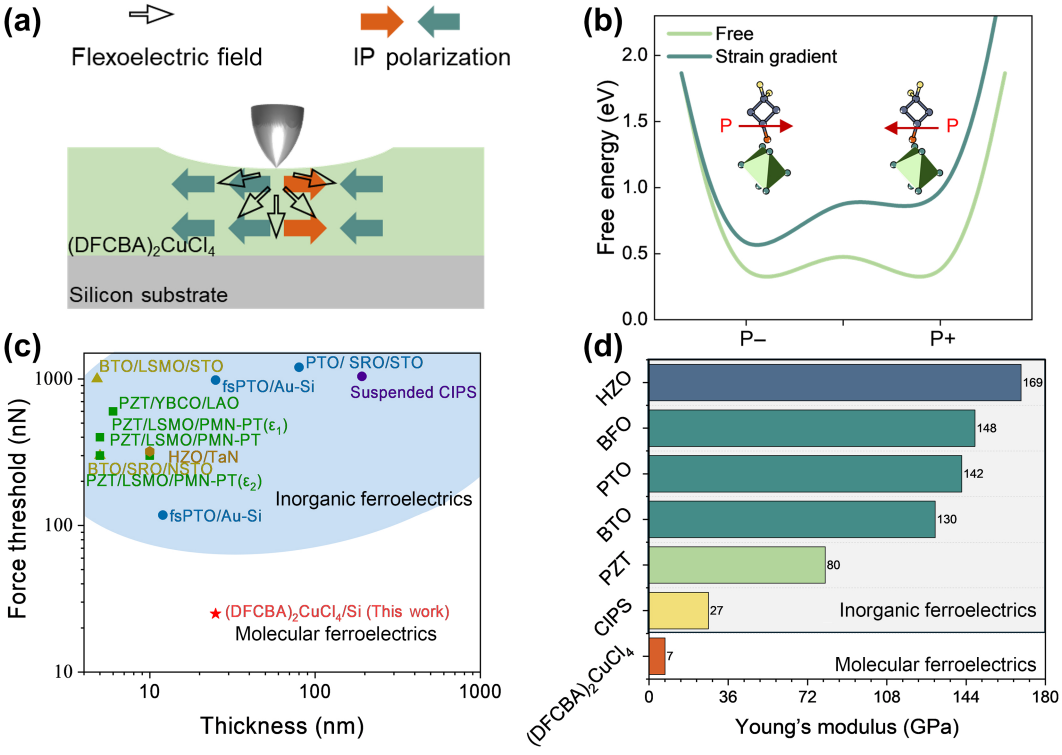

Figure 4 Mechanism of mechanical switching and ultralow switching force. (a) Schematic of the flexoelectric field and corresponding polarization switching in a $(DFCBA)_2CuCl_4$ NS under a PFM tip with static force. (b) Double-well potential of Landau free energy with strain-free state (light green curve) and with IP strain gradient state (green curve). (c) Summary of force threshold and thickness for mechanical switching in several ferroelectric membranes reported to date [12, 13, 15–22, 43, 45]. (d) Summary of Young's modulus of ferroelectrics [49–53] in (c).

response of the nanosheet under an AFM tip can be reasonably described by the Hertz contact model [55, 56]. According to this model, the indentation depth h and contact radius a scale with the elastic modulus as $h \propto E^{*-2/3}$ and $a \propto E^{*-1/3}$ under a given applied force. These relations indicate that a lower elastic modulus leads to larger deformation and an expanded contact region, which promotes the formation of a stronger strain gradient beneath the tip. Since the flexoelectric field is directly related to the strain gradient, this provides a physical basis for the reduced switching force observed in our system. Whereas force-induced switching in most inorganic oxide ferroelectrics is typically confined to ultrathin regimes (< 20 nm) [16, 20, 42], $(DFCBA)_2CuCl_4$ supports reliable switching even at thicknesses exceeding 200 nm, highlighting a distinct mechanical switching landscape enabled by its compliance molecular lattice. At the same time, this flexibility distinguishes the material from conventional high-modulus oxide ferroelectrics and may be accompanied by trade-offs in properties, including a lower polarization magnitude and Curie temperature (Table S1 in the ESM). Rather than serving as a direct replacement for inorganic oxide ferroelectrics, $(DFCBA)_2CuCl_4$ is better positioned as a complementary platform for applications that benefit from strong electromechanical coupling at low stress such as pressure sensing, ultrasonic catalysis, and mechanical energy harvesting.

To further investigate the strain gradient behavior of different ferroelectrics under identical loading conditions, we conducted finite element simulations on $(DFCBA)_2CuCl_4$, as well as classical ferroelectrics such as BTO and PZT (Fig. 5). Under an applied force of 35 nN on a 35 nm-thick nanosheet, $(DFCBA)_2CuCl_4$ exhibited a maximum out-of-plane displacement of 0.8 nm—nearly four times that in conventional ferroelectrics

In addition, $(DFCBA)_2CuCl_4$ showed a broader strain distribution and a significantly larger and more spatially extended strain gradient. These characteristics contribute to the generation of a stronger and more widespread flexoelectric field, enabling effective and efficient domain switching. The magnitude of the induced flexoelectric field (E) can be estimated as follows [57–60]

$$E = \frac{\lambda e}{\varepsilon_0 a_j} \frac{\partial e_{ij}}{\partial x_k} \quad (1)$$

where e is the electron charge and a_j is the lattice constant, λ is the proportionality coefficient, ε_0 is vacuum permittivity, and $\partial e_{ij}/\partial x_k$ is the strain gradient, respectively. Based on the simulation results, the strain gradient is estimated to be ~ 2×10^6 m^{-1}. Taking a conservative value of λ = 1, the resulting flexoelectric field is calculated to be 47.9 MV·m^{-1}, significantly surpassing the coercive field (1.2 MV·m^{-1}) of $(DFCBA)_2CuCl_4$, thereby enabling effective polarization switching.

Given the extremely low force required for mechanical polarization switching in this system, we hypothesized that the flexoelectric field generated by ultrasonic excitation could also influence ferroelectric domain configurations. To examine this possibility, we compared the ferroelectric domain configurations of the nanosheets before and after 1 min of ultrasonic treatment in air. As shown in Fig. 6, noticeable changes in domain shapes and sizes are observed after ultrasound exposure, while the surface morphology remains essentially unchanged. These results indicate that ultrasound can induce domain modification in the molecular ferroelectric nanosheets. Previous studies, such as the work by Huang et al. [50], reported that ultrasonic excitation in the air for 20 min led only to limited domain modification in PMN-PT, and that

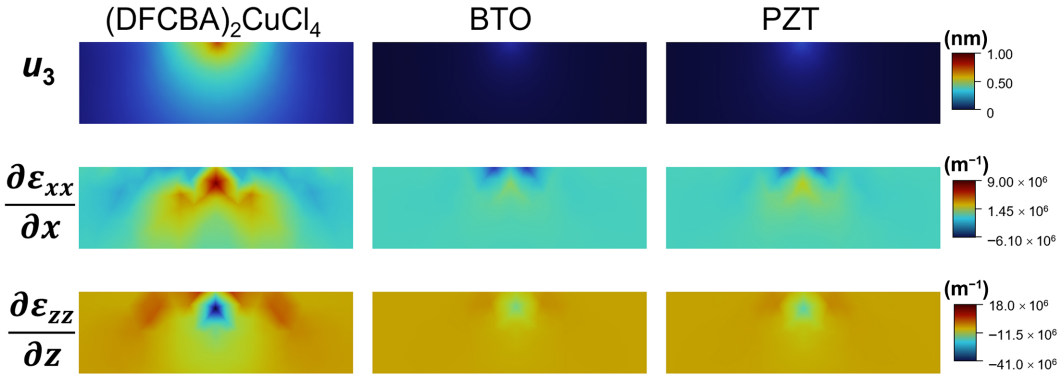

Figure 5 Finite element simulation of displacement and strain gradient $(DFCBA)_2CuCl_4$ BTO, and PZT under a 35 nN load.

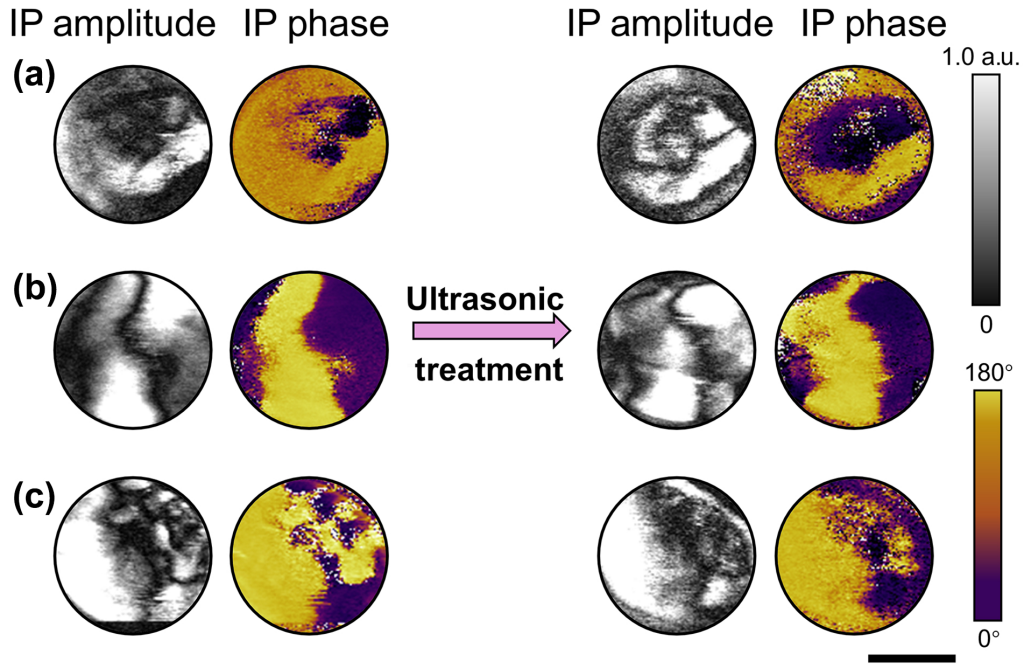

Figure 6 Ultrasound-induced domain modification in $(DFCBA)_2CuCl_4$ NSs before and after ultrasonic exposure for 1 min in the air. Scale bar: 200 nm

effective polarization reconfiguration required aqueous environments where H^+/OH^- ions provide efficient charge screening. In contrast, in our system, the mechanical force threshold for domain switching is sufficiently low that the flexoelectric field generated by ultrasound alone can induce appreciable domain reconfiguration, even in the air.

3 Summary

In summary, we have demonstrated ultralow-force polarization switching in two-dimensional molecular ferroelectric $(DFCBA)_2CuCl_4$ nanosheets. Polarization reversal is achieved with forces as low as 25 nN, corresponding to local pressures below 20 MPa—far smaller than those required for inorganic oxides. This ultralow threshold arises from the flexible molecular lattice, enabling large strain gradients and strong flexoelectric responses under minimal stress. This capability not only minimizes the mechanical damage that may arise during force-induced switching but also underscores the feasibility of using mechanical domain patterning techniques, such as nanoimprint lithography, to construct large-area periodic domain structures.

4 Materials and methods

4.1 Synthesis of 2D $(DFCBA)_2CuCl_4$ nanosheets (NSs)

The (3,3-difluorocyclobutylammonium)Cl ([DFCBA]Cl) and $CuCl_2$ are commercially available. In a typical synthesis of $(DFCBA)_2CuCl_4$ nanosheets, 0.1 mmol of (DFCBA)Cl and 0.05 mmol of $CuCl_2$ were dissolved in 2 mL of DMF (Meryer, 99.8%, SuperDry) to prepare a perovskite precursor solution at room temperature. Next, 15 μL of this precursor solution was rapidly added to 10 mL of toluene under vigorous stirring. The nanosheets formed instantly, causing the solution to turn yellow-green. The $(DFCBA)_2CuCl_4$ nanosheets were then collected by centrifugation at 3000 RCF for 1 min. Finally, the nanosheets were redispersed in toluene for further characterization.

4.2 Material characterization

Samples for TEM, XRD, and XPS analysis were prepared by depositing a nanosheet colloidal dispersion in toluene onto amorphous carbon-coated copper grids (for TEM), glass slides (for XRD), and silicon substrates (for XPS), followed by drying at 333 K. XRD patterns were recorded using a Rigaku SmartLab SE

diffractometer with Cu Kα radiation (λ = 1.5406 Å, 40 kV, 40 mA). TEM and EDS mapping images were obtained with a Talos F200X microscope. XPS measurements were carried out on a Thermo Scientific K-Alpha system with Al Kα radiation ($h\nu$ = 1486.6 eV), using a 400 μm spot size, 12 kV voltage, and 6 mA filament current. Full scans were acquired with a pass energy of 150 eV and a step size of 1 eV, while narrow scans used 50 eV pass energy and 0.1 eV step size.

4.3 PFM measurements and mechanical domain switching

The NSs colloidal dispersion in toluene was spin-coated onto a highly doped silicon substrate and dried at 333 K, before PFM measurements. The ferroelectric domain structures of these nanosheets were examined using PFM (Asylum Research MFP-3D) with conductive probes. First, the spring constant (k) and inverse optical lever sensitivity of the AFM probes (PPP-EFM, Nanosensors, with $k \approx 2.5$ N·m^{-1}) were calibrated via the thermal noise method. The electrically grounded AFM tip was then positioned at the center of the NSs, where a localized vertical force was applied. The force was controlled using the AFM force-curve mode, and the loading/unloading velocity of the AFM cantilever was set to 100 nm·s^{-1} to avoid surface damage. The trigger force was pre-set via the setpoint value, and once the force reached this value, it was maintained for 1 s before unloading. For PFM measurements, to minimize interference to ferroelectric domains, the AFM cantilever was excited with an AC voltage of 0.7 V, with the tip-surface contact force set to approximately 20 nN. To enhance PFM sensitivity, a dual-frequency resonance-tracking technique, also provided by Asylum Research, was employed [61].

4.4 Stress–strain simulation

The stress–strain simulation was performed using the Solid Mechanics module in COMSOL Multiphysics. A perovskite thin film (400 nm × 400 nm × 35 nm) was modeled on a fixed silicon (100) substrate (400 nm × 400 nm × 500 nm), with the bottom surface fully constrained. A 35 nN load was applied via a conical Si tip with a spherical apex (radius = 25 nm) at the film's center. To reduce computational cost, a quarter-symmetric model was constructed by cutting the geometry along the central axis, and symmetry conditions were applied to the cut surfaces. The full three-dimensional (3D) solution was obtained by mirroring the quarter-model results. Mesh refinement was applied near the contact region to ensure accuracy.

4.5 Acoustic domain switching

The nanosheets spin-coated on Si substrates were first characterized by PFM to obtain their initial domain structures. They were then placed in a sealed glass vial and subjected to 1 min of ultrasonic treatment using an ultrasonic cleaner. Finally, the domain structures after ultrasound exposure were characterized.

Electronic Supplementary Material: Supplementary material (supplementary information on synthesis and characterization for NSs, detailed PFM images for mechanical domain switching, nanoindentation measurements and comparison of functional properties) is available in the online version of this article at https://doi.org/10.26599/NR.2026.94908742.

Data availability

All data needed to support the conclusions in the paper are presented in the manuscript and the Electronic Supplementary Material. Additional data related to this paper may be requested from the corresponding author upon request.

Acknowledgements

This work was supported by the National Natural Science Foundation of China (Nos. 224B2502, 223B2502, and 22405039) and the National Key Research and Development Program of China (No. 2024YFA1509300). We would like to thank Prof. Xian-Jiang Song (Nanchang University) for his insightful comments and helpful suggestions that greatly improved the manuscript.

Declaration of competing interest

All the contributing authors report no conflict of interest in this work.

Author contribution statement

Y.-M. Y., H. H. H., W. Z., and Q. P.: Conceptualization. T.-T. S., Z.-J. F., and X. Z.: Methodology. T.-T. S., Z.-J. F., X. Z., X.-X. C., Y.-A. X., and H.-R. J.: Investigation. T.-T. S. and Q. P.: Visualization. Y.-M. Y., W. Z., Q. P., H. H. H.: Data curation & analysis. Y.-M. Y., H. H. H., W. Z., and Q. P.: Supervision. T.-T. S., Q. P., and Y.-M. Y.: Writing – original draft. All authors: Writing – review & editing.

Use of AI statement

None.

References

[1] Scott, J. F. Applications of modern ferroelectrics. *Science* **2007**, *315*, 954–959.

[2] Neese, B.; Chu, B. J.; Lu, S. G.; Wang, Y.; Furman, E.; Zhang, Q. M. Large electrocaloric effect in ferroelectric polymers near room temperature. *Science* **2008**, *321*, 821–823.

[3] Abdelwahab, I.; Tilmann, B.; Wu, Y. Z.; Giovanni, D.; Verzhbitskiy, I.; Zhu, M. L.; Berté, R.; Xuan, F. Y.; de S. Menezes, L.; Eda, G. et al. Giant second-harmonic generation in ferroelectric $NbOI_2$. *Nat. Photonics* **2022**, *16*, 644–650.

[4] Lu, T.; Xue, J. Y.; Shen, P. H.; Liu, H. F.; Gao, X. Y.; Li, X. M.; Hao, J.; Huang, D. P.; Zhao, R. T.; Yan, J. L. et al. Two-dimensional fully ferroelectric-gated hybrid computing-in-memory hardware for high-precision and energy-efficient dynamic tracking. *Sci. Adv.* **2024**, *10*, eadp0174.

[5] Song, C. M.; Kim, D.; Lee, S.; Kwon, H. J. Ferroelectric 2D SnS_2 analog synaptic FET. *Adv. Sci.* **2024**, *11*, 2308588.

[6] You, L.; Liu, F. C.; Li, H. S.; Hu, Y. Z.; Zhou, S.; Chang, L.; Zhou, Y.; Fu, Q. D.; Yuan, G. L.; Dong, S. et al. In-plane ferroelectricity in thin flakes of van der Waals hybrid perovskite. *Adv. Mater.* **2018**, *30*, 1803249.

[7] Balke, N.; Choudhury, S.; Jesse, S.; Huijben, M.; Chu, Y. H.; Baddorf, A. P.; Chen, L. Q.; Ramesh, R.; Kalinin, S. V. Deterministic control of ferroelastic switching in multiferroic materials. *Nat. Nanotechnol.* **2009**, *4*, 868–875.

[8] Song, X. J.; Xiong, Y. A.; Zhou, R. J.; Cao, X. X.; Jing, Z. Y.; Ji, H. R.; Gu, Z. X.; Sha, T. T.; Xiong, R. G.; You, Y. M. The first demonstration of strain-controlled periodic ferroelectric domains with

superior piezoelectric response in molecular materials. *Adv. Mater.* **2023**, *35*, 2211584.
[9] Ma, J.; Ma, J.; Zhang, Q. H.; Peng, R. C.; Wang, J.; Liu, C.; Wang, M.; Li, N.; Chen, M. F.; Cheng, X. X. et al. Controllable conductive readout in self-assembled, topologically confined ferroelectric domain walls. *Nat. Nanotechnol.* **2018**, *13*, 947–952.
[10] Tian, G.; Yang, W. D.; Song, X.; Zheng, D. F.; Zhang, L. Y.; Chen, C.; Li, P. L.; Fan, H.; Yao, J. X.; Chen, D. Y. et al. Manipulation of conductive domain walls in confined ferroelectric nanoislands. *Adv. Funct. Mater.* **2019**, *29*, 1807276.
[11] Xiong, Y. A.; Gu, Z. X.; Song, X. J.; Yao, J.; Pan, Q.; Feng, Z. J.; Du, G. W.; Ji, H. R.; Sha, T. T.; Xiong, R. G. et al. Rational design of molecular ferroelectrics with negatively charged domain walls. *J. Am. Chem. Soc.* **2022**, *144*, 13806–13814.
[12] Park, S. M.; Wang, B.; Das, S.; Chae, S. C.; Chung, J. S.; Yoon, J. G.; Chen, L. Q.; Yang, S. M.; Noh, T. W. Selective control of multiple ferroelectric switching pathways using a trailing flexoelectric field. *Nat. Nanotechnol.* **2018**, *13*, 366–370.
[13] Lu, H.; Bark, C. W.; Esque de los Ojos, D.; Alcala, J.; Eom, C. B.; Catalan, G.; Gruverman, A. Mechanical writing of ferroelectric polarization. *Science* **2012**, *336*, 59–61.
[14] Liu, H.; Lai, Q. L.; Fu, J.; Zhang, S. J.; Fu, Z. M.; Zeng, H. L. Reversible flexoelectric domain engineering at the nanoscale in van der Waals ferroelectrics. *Nat. Commun.* **2024**, *15*, 4556.
[15] Lun, Y. Z.; Wang, X. Y.; Kang, J. Q.; Ren, Q.; Wang, T. J.; Han, W. X.; Gao, Z. Y.; Huang, H. B.; Chen, Y. B.; Chen, L. Q. et al. Ultralow tip-force driven sizable-area domain manipulation through transverse flexoelectricity. *Adv. Mater.* **2023**, *35*, 2302320.
[16] Guan, Z.; Li, Y. K.; Zhao, Y. F.; Peng, Y.; Han, G. Q.; Zhong, N.; Xiang, P. H.; Chu, J. H.; Duan, C. G. Mechanical polarization switching in $Hf_{0.5}Zr_{0.5}O_2$ thin film. *Nano Lett.* **2022**, *22*, 4792–4799.
[17] Lu, H.; Kim, D. J.; Bark, C. W.; Ryu, S.; Eom, C. B.; Tsymbal, E. Y.; Gruverman, A. Mechanically-induced resistive switching in ferroelectric tunnel junctions. *Nano Lett.* **2012**, *12*, 6289–6292.
[18] Lu, H. D.; Liu, S.; Ye, Z. Y.; Yasui, S.; Funakubo, H.; Rappe, A. M.; Gruverman, A. Asymmetry in mechanical polarization switching. *Appl. Phys. Lett.* **2017**, *110*, 222903.
[19] Gonzalez Casal, S.; Bai, X. F.; Alhada-Lahbabi, K.; Canut, B.; Vilquin, B.; Rojo Romeo, P.; Brottet, S.; Albertini, D.; Deleruyelle, D.; Bugnet, M. et al. Mechanical switching of ferroelectric domains in 33–200 nm-thick sol–gel-grown $PbZr_{0.2}Ti_{0.8}O_3$ films assisted by nanocavities. *Adv. Electron. Mater.* **2022**, *8*, 2200077.
[20] Guo, E. J.; Roth, R.; Das, S.; Dörr, K. Strain induced low mechanical switching force in ultrathin $PbZr_{0.2}Ti_{0.8}O_3$ films. *Appl. Phys. Lett.* **2014**, *105*, 012903.
[21] Vats, G.; Ravikant; Schoenherr, P.; Kumar, A.; Seidel, J. Low-pressure mechanical switching of ferroelectric domains in $PbZr_{0.48}Ti_{0.52}O_3$. *Adv. Electron. Mater.* **2020**, *6*, 2000523.
[22] Yang, X. R.; Han, L.; Ning, H. K.; Xu, S. Q.; Hao, B.; Li, Y. C.; Li, T. T.; Gao, Y.; Yan, S. J.; Li, Y. Y. et al. Ultralow-pressure-driven polarization switching in ferroelectric membranes. *Nat. Commun.* **2024**, *15*, 9281.
[23] Liu, H. Y.; Zhang, H. Y.; Chen, X. G.; Xiong, R. G. Molecular design principles for ferroelectrics: Ferroelectrochemistry. *J. Am. Chem. Soc.* **2020**, *142*, 15205–15218.
[24] Pan, Q.; Gu, Z. X.; Zhou, R. J.; Feng, Z. J.; Xiong, Y. A.; Sha, T. T.; You, Y. M.; Xiong, R. G. The past 10 years of molecular ferroelectrics: Structures, design, and properties. *Chem. Soc. Rev.* **2024**, *53*, 5781–5861.
[25] Zhang, H. Y.; Tang, Y. Y.; Shi, P. P.; Xiong, R. G. Toward the targeted design of molecular ferroelectrics: Modifying molecular symmetries and homochirality. *Acc. Chem. Res.* **2019**, *52*, 1928–1938.
[26] Pan, Q.; Xiong, Y. A.; Sha, T. T.; Feng, Z. J.; Zhou, R. J.; Yao, J.; Hu, H. H.; You, Y. M. Strain-induced tunable enhancement of piezoelectricity in a novel molecular multiferroic material. *Adv. Mater.* **2025**, *37*, 2410585.
[27] Xie, Y. F.; Ai, Y.; Zeng, Y. L.; He, W. H.; Huang, X. Q.; Fu, D. W.; Gao, J. X.; Chen, X. G.; Tang, Y. Y. The soft molecular polycrystalline ferroelectric realized by the fluorination effect. *J. Am. Chem. Soc.* **2020**, *142*, 12486–12492.
[28] Ai, Y.; Zeng, Y. L.; He, W. H.; Huang, X. Q.; Tang, Y. Y. Six-fold vertices in a single-component organic ferroelectric with most equivalent polarization directions. *J. Am. Chem. Soc.* **2020**, *142*, 13989–13995.
[29] Huang, C. R.; Luo, X. Z.; Chen, X. G.; Song, X. J.; Zhang, Z. X.; Xiong, R. G. A multiaxial lead-free two-dimensional organic-inorganic perovskite ferroelectric. *Natl. Sci. Rev.* **2021**, *8*, nwaa232.
[30] Yang, S.; Niu, W. X.; Wang, A. L.; Fan, Z. X.; Chen, B.; Tan, C. L.; Lu, Q. P.; Zhang, H. Ultrathin two-dimensional organic-inorganic hybrid perovskite nanosheets with bright, tunable photoluminescence and high stability. *Angew. Chem., Int. Ed.* **2017**, *56*, 4252–4255.
[31] Sha, T. T.; Zhang, X. C.; Zhou, R. J.; Du, G. W.; Xiong, Y. A.; Pan, Q.; Yao, J.; Feng, Z. J.; Gao, X. S.; You, Y. M. Organic–inorganic hybrid perovskite ferroelectric nanosheets synthesized by a room-temperature antisolvent method. *Adv. Sci.* **2024**, *11*, 2400636.
[32] Hu, H. H.; Jing, Z. Y.; Pan, Q.; Sha, T. T.; Ji, H. R.; Cao, X. X.; Song, X. J.; Feng, Z. J.; Yao, J.; Zhou, R. J. et al. Organic–inorganic hybrid perovskite for ferroelectric catalysis. *Adv. Mater.* **2024**, *36*, 2413547.
[33] Aizu, K. Possible species of "ferroelastic" crystals and of simultaneously ferroelectric and ferroelastic crystals. *J. Phys. Soc. Jpn.* **1969**, *27*, 387–396.
[34] Zhu, L. J.; Zhang, H. Y.; Lu, Q. P.; Wang, Y.; Deng, Z. B.; Hu, Y. F.; Lou, Z. D.; Cui, Q. H.; Hou, Y. B.; Teng, F. Synthesis of ultrathin two-dimensional organic–inorganic hybrid perovskite nanosheets for polymer field-effect transistors. *J. Mater. Chem. C* **2018**, *6*, 3945–3950.
[35] Biesinger, M. C. Advanced analysis of copper X-ray photoelectron spectra. *Surf. Interface Anal.* **2017**, *49*, 1325–1334.
[36] Weidman, M. C.; Seitz, M.; Stranks, S. D.; Tisdale, W. A. Highly tunable colloidal perovskite nanoplatelets through variable cation, metal, and halide composition. *ACS Nano* **2016**, *10*, 7830–7839.
[37] Yuan, B.; Yu, Y. High-resolution transmission electron microscopy of beam-sensitive halide perovskites. *Chem* **2022**, *8*, 327–339.
[38] De Trizio, L.; Infante, I.; Abdelhady, A. L.; Brovelli, S.; Manna, L. Guidelines for the characterization of metal halide nanocrystals. *Trends Chem.* **2021**, *3*, 631–644.
[39] Sha, T. T.; Xiong, Y. A.; Pan, Q.; Chen, X. G.; Song, X. J.; Yao, J.; Miao, S. R.; Jing, Z. Y.; Feng, Z. J.; You, Y. M. et al. Fluorinated 2D lead iodide perovskite ferroelectrics. *Adv. Mater.* **2019**, *31*, 1901843.
[40] Higgins, M. J.; Proksch, R.; Sader, J. E.; Polcik, M.; Mc Endoo, S.; Cleveland, J. P.; Jarvis, S. P. Noninvasive determination of optical lever sensitivity in atomic force microscopy. *Rev. Sci. Instrum.* **2006**, *77*, 013701.
[41] Haugstad, G. *Atomic Force Microscopy: Understanding Basic Modes and Advanced Applications*; Wiley: Hoboken, 2012.
[42] Wang, B.; Lu, H. D.; Bark, C. W.; Eom, C. B.; Gruverman, A.; Chen, L. Q. Mechanically induced ferroelectric switching in $BaTiO_3$ thin films. *Acta Mater.* **2020**, *193*, 151–162.
[43] Gu, Y. J.; Hong, Z. J.; Britson, J.; Chen, L. Q. Nanoscale mechanical switching of ferroelectric polarization via flexoelectricity. *Appl. Phys. Lett.* **2015**, *106*, 022904.
[44] Liang, X.; Dong, H. T.; Wang, Y. F.; Ma, Q. Q.; Shang, H. X.; Hu, S. L.; Shen, S. P. Advancements of flexoelectric materials and their implementations in flexoelectric devices. *Adv. Funct. Mater.* **2024**, *34*, 2409906.
[45] Wang, J.; Fang, H.; Nie, F.; Chen, Y. N.; Tian, G.; Shi, C. Q.; He, B.; Lü, W. M.; Zheng, L. M. Domain switching in $BaTiO_3$ films induced by an ultralow mechanical force. *ACS Appl. Mater. Interfaces* **2022**, *14*, 48917–48925.
[46] Niharika, Y.; Dhirendra Singh, Y.; Preeti, V.; Rajesh Chandra, G. Electronic and mechanical properties of chemical bonds (A–O &

B–O) in cubic phase $A^{+2}B^{+4}O_3$ perovskite oxides. *Am. J. Phys. Appl.* **2023**, *11*, 80–88.

[47] Xiong, Y. A.; Feng, Z. J.; Jing, Z. Y.; Pan, Q.; Sha, T. T.; Miao, S. R.; Yao, J.; Du, G. W.; You, Y. M. Recent progress in molecular ferroelectrics with perovskite structure. *Chin. Sci. Bull.* **2020**, *65*, 916–930.

[48] Zhang, T.; Xu, K.; Li, J.; He, L.; Fu, D. W.; Ye, Q.; Xiong, R. G. Ferroelectric hybrid organic-inorganic perovskites and their structural and functional diversity. *Natl. Sci. Rev.* **2023**, *10*, nwac240.

[49] Chen, C. T.; Lin, S. C.; Trstenjak, U.; Spreitzer, M.; Wu, W. J. Comparison of metal-based PZT and PMN-PT energy harvesters fabricated by aerosol deposition method. *Sensors* **2021**, *21*, 4747.

[50] Maruyama, K.; Kawakami, Y.; Narita, F. Young's modulus and ferroelectric property of $BaTiO_3$ films formed by aerosol deposition in consideration of residual stress and film thickness. *Jpn. J. Appl. Phys.* **2022**, *61*, SN1011.

[51] Jian, S. R.; Chang, H. W.; Tseng, Y. C.; Chen, P. H.; Juang, J. Y. Structural and nanomechanical properties of $BiFeO_3$ thin films deposited by radio frequency magnetron sputtering. *Nanoscale Res. Lett.* **2013**, *8*, 297.

[52] Li, Z.; Grimsditch, M.; Foster, C. M.; Chan, S. K. Dielectric and elastic properties of ferroelectric materials at elevated temperature. *J. Phys. Chem. Solids* **1996**, *57*, 1433–1438.

[53] Bolotov, L.; Migita, S.; Fujio, R.; Ishimaru, M.; Hatayama, S.; Uchida, N. Impact of annealing on electric and elastic properties of 10-nm $Hf_{0.5}Zr_{0.5}O_2$ films prepared on Si by sputtering. *Microelectron. Eng.* **2022**, *258*, 111770.

[54] Zhang, X. P.; Jiang, X. A.; Du, G. S.; Ren, Q.; Zhu, W. F.; Kang, J. Q.; Lun, Y. Z.; Wang, T. J.; Bai, B. F.; Yu, Z. X. et al. Elastic properties and Ion-mediated domain switching of self-assembled heterostructures $CuInP_2S_6$-$In_{4/3}P_2S_6$. *Microstructures* **2023**, *3*, 2023010.

[55] Fischer-Cripps, A. C. *Introduction to Contact Mechanics*; Springer: New York, 2000.

[56] Johnson, K. L. *Contact Mechanics*; Cambridge University Press: Cambridge, 1987.

[57] Jeon, B. C.; Lee, D.; Lee, M. H.; Yang, S. M.; Chae, S. C.; Song, T. K.; Bu, S. D.; Chung, J. S.; Yoon, J. G.; Noh, T. W. Flexoelectric effect in the reversal of self-polarization and associated changes in the electronic functional properties of $BiFeO_3$ thin films. *Adv. Mater.* **2013**, *25*, 5643–5649.

[58] Lee, D.; Yoon, A.; Jang, S. Y.; Yoon, J. G.; Chung, J. S.; Kim, M.; Scott, J. F.; Noh, T. W. Giant flexoelectric effect in ferroelectric epitaxial thin films. *Phys. Rev. Lett.* **2011**, *107*, 057602.

[59] Resta, R. Towards a bulk theory of flexoelectricity. *Phys. Rev. Lett.* **2010**, *105*, 127601.

[60] Tian, S. L.; Wang, C.; Zhou, Y.; Feng, Y.; Yao, X. K.; Ge, C.; He, M.; Yang, G. Z.; Jin, K. J. Effect of mechanical force on domain switching in $BiFeO_3$ ultrathin films. *Sci. China Phys., Mech. Astron.* **2020**, *63*, 217711.

[61] Zhao, L. N.; Lu, Z. X.; Zhang, F. Y.; Tian, G.; Song, X.; Li, Z. W.; Huang, K. R.; Zhang, Z.; Qin, M. H.; Wu, S. J. et al. Current rectifying and resistive switching in high density $BiFeO_3$ nanocapacitor arrays on Nb–$SrTiO_3$ substrates. *Sci. Rep.* **2015**, *5*, 9680.